RESEARCH ARTICLE

Check for updates

ADVANCED
FUNCTIONAL
MATERIALS
www.afm-journal.de

From Amorphous to Polycrystalline Rubrene: Charge Transport in Organic Semiconductors Paralleled with Silicon

Julie Euvrard,* Oki Gunawan, Antoine Kahn, and Barry P. Rand*

While progress has been made in the design of organic semiconductors (OSCs) with improved transport properties, the understanding of the mechanisms involved is still limited, hindering further development. In this study, the interplay between structural order and transport considering one single OSC, analogous to past research on silicon is investigated. Rubrene ($C_{42}H_{28}$) is selected as it spans transport mechanisms from thermally activated hopping in its amorphous form to band-like in highly ordered crystals in the orthorhombic polymorph. Transport characterizations including variable temperature conductivity, advanced Hall effect, and magnetoresistance measurements are performed on rubrene films with varying levels of order (polycrystalline vs amorphous), crystal phase (orthorhombic vs triclinic), and morphologies (platelet-like vs spherulitic grains). A conductivity tuning range over four orders of magnitude between polycrystalline (platelet-like) orthorhombic and amorphous films is reported. As observed in silicon, transport in polycrystalline orthorhombic rubrene is limited by energy barriers at grain boundaries. Additionally, a gradual transition from predominantly band-like to predominantly hopping transport with increasing disorder, reminiscent of observations in silicon is shown. Nevertheless, OSCs differ from covalently bonded silicon by their weak intermolecular interaction. This study highlights that molecular packing must be optimized in OSCs to favor advantageous π-orbital overlap and optimized transport properties.

1. Introduction

Conductive polymers and small molecules forming the category of organic semiconductors (OSCs) have been studied since the late 1970s,[1] finding applications in a wide range of technologies such as solar cells,[2] organic light-emitting diodes (OLEDs)[3,4]

J. Euvrard, A. Kahn, B. P. Rand
Department of Electrical and Computer Engineering
Princeton University
Princeton, NJ 08544, USA
E-mail: julie.euvrard@princeton.edu; brand@princeton.edu
J. Euvrard, B. P. Rand
Andlinger Center for Energy and the Environment
Princeton University
Princeton, NJ 08544, USA
O. Gunawan
IBM T. J. Watson Research Center
Yorktown Heights
New York, NY 10598, USA

The ORCID identification number(s) for the author(s) of this article can be found under https://doi.org/10.1002/adfm.202206438.

and transistors.[5] Principal advantages of OSCs over their inorganic counterparts include the potential for low-cost, large area, semi- or fully-transparent, and flexible devices.[6] While the OLED industry has flourished in the last two decades,[7] the rise of other technologies is hindered by limitations encountered in OSC-based devices. In particular, OSCs suffer from inefficient transport properties due to the intrinsic nature of these semiconductors. Contrary to crystalline silicon which features covalent bonding and band charge transport, OSCs are mostly encountered in a disordered structure, and interactions between molecules are weak. Significant progress has been made in the design of OSCs with improved transport properties leading to an impressive rise in charge carrier mobility.[8] Yet, our understanding of charge transport in OSCs is still unclear despite a rich literature on the subject with both experimental and theoretical studies. Our lack of comprehension is in part due to the inherent difficulty when comparing different OSCs with varying molecular structures. While some polymers and molecular films exhibit a strong localization of charge carriers on molecular sites leading to a hopping transport process, a few organic crystals are capable of delocalized "band-like" transport similar to crystalline inorganic semiconductors.[9–11] As it has been conducted for silicon with variations in morphology from single crystals to fully amorphous films, it would be of particular interest to analyze the impact of order, packing, and morphology within one single organic molecule. Our goal is to understand what parameters are important to achieve efficient transport and how they influence it. In silicon, it is established that grain boundaries and disorder are the main culprits for degradation in carrier mobility.[12,13] We may wonder whether a similar conclusion is accurate in a molecular framework with weak intermolecular van der Waals forces.

To answer this question comprehensively, it is ideal to access various crystal phases, levels of order, and morphologies without changing the chemical nature of the molecule. This is achieved in this work using 5,6,11,12-tetraphenyltetracene ($C_{42}H_{28}$), more commonly known as rubrene, a benchmark OSC notable for achieving band-like transport properties in single crystals,[14–17] while hopping transport is expected in its amorphous form. Additionally, we take advantage of the ability

to achieve high-quality polycrystalline films of rubrene with varying crystal phases (orthorhombic and triclinic) and morphologies (platelet-like and spherulitic grains).[18,19] Variable temperature conductivity measurements along with Urbach energy extraction are performed to provide an understanding of the impact of order and morphology on transport properties. In addition, the use of advanced Hall measurement, for the first time performed on OSC thin films without the use of "gating" (gate voltage applied through the addition of a dielectric and gate electrode above the channel), provides access to the intrinsic properties of rubrene and the degree of carrier localization. A simplified Gaussian distribution model is solved analytically to conclude on the transport mechanisms.

Our results highlight similarities between organic semiconductors and silicon, two types of semiconductors often contrasted with each other. Polycrystalline rubrene in its orthorhombic crystal phase behaves similarly to polycrystalline silicon, where transport is band-like and energy barriers at grain boundaries limit its efficiency. A hole carrier density and mobility of $\approx 10^{15}$ cm^{-3} and ≈ 2 cm^2 V^{-1} s^{-1}, respectively, is measured by the Hall effect in polycrystalline orthorhombic films (with platelet morphology). As the disorder is drastically increased to reach a fully amorphous film of rubrene, conductivity drops by over four orders of magnitude, similarly to amorphous silicon. Despite the high resistivity, we are able to detect a Hall signal in amorphous rubrene, suggesting the presence of a small density of delocalized carriers where localized carriers dominate. Hall and magnetoresistance measurements give evidence for a gradual transition from predominantly band-like transport to predominantly hopping transport as the order is decreased within the crystal grains in the orthorhombic phase. While the impact of the order on transport properties of rubrene is reminiscent of silicon, our work highlights that packing plays a key role in molecular films organized through weak intermolecular forces as opposed to covalently bonded inorganic crystals. In particular, we show that the triclinic polymorph of rubrene exhibits transport properties akin to the amorphous film, despite an increase in order. Overall, our study suggests that packing, over order, is paramount for charge transport in organic semiconductor thin films.

2. Results

2.1. From Amorphous to Polycrystalline Rubrene Thin Films

An underlayer of tris[4-(5-phenylthiophen-2-yl)-phenyl]amine (TPTPA) is used to allow the crystallization of rubrene films into various phases and morphologies.[18] **Figure 1**a–c displays the polarized optical microscope (POM) images of 100 nm rubrene films crystallized in the orthorhombic (Figure 1a,b) or triclinic phase (Figure 1c). By tuning the annealing temperature, the morphology of the orthorhombic films can additionally be tuned between platelets (i.e., each grain is a single-domain crystallite) and spherulites (i.e., polycrystalline branching leading to misoriented crystal regions). Homoepitaxy is used to increase the thickness of the orthorhombic crystalline template (20 nm) to its final thickness (100 nm).[19] The preservation of the crystalline structure through homoepitaxy is verified with atomic force microscopy (AFM) shown in Figure S1 (Supporting Information). Triclinic films are directly obtained upon annealing
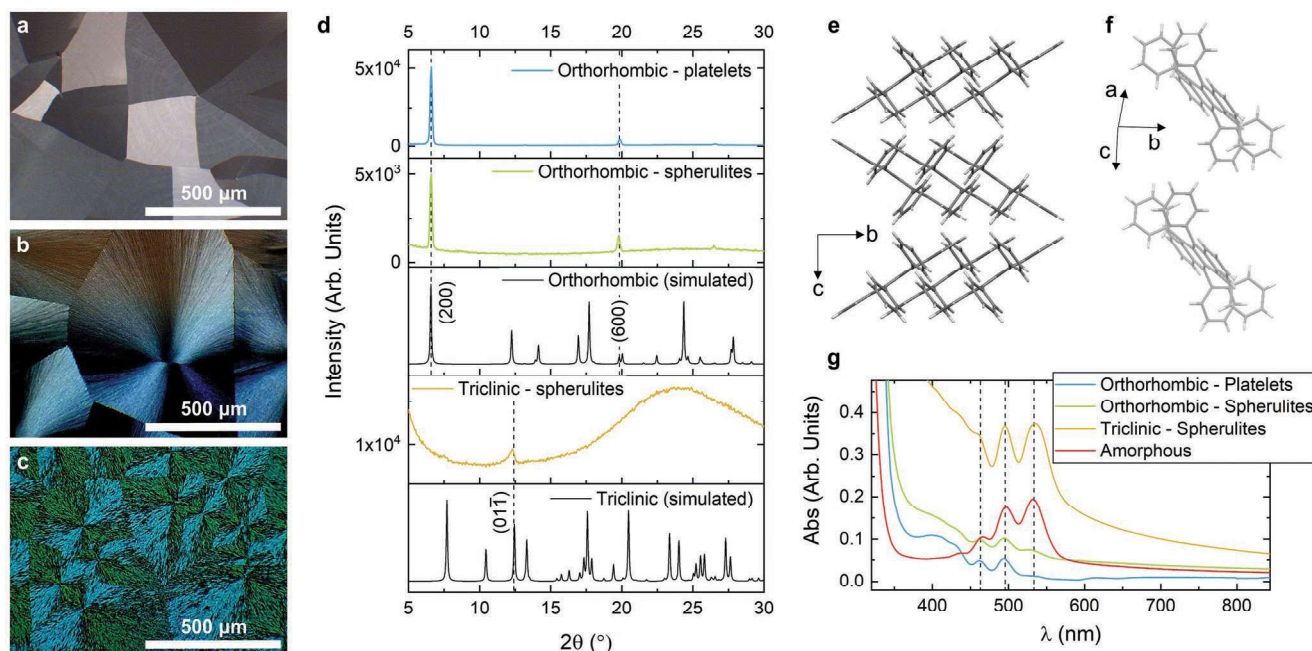

Figure 1. POM images of a) orthorhombic platelets, b) orthorhombic spherulites, and c) triclinic spherulites rubrene thin films (100 nm thick). d) Experimental XRD patterns of the films studied compared to the simulated patterns for orthorhombic and triclinic rubrene powder. Molecular packing of e) orthorhombic (herringbone packing) and f) triclinic rubrene. The simulated XRD patterns and molecular packing are obtained from the Cambridge Structural Database (CSD) and the freeware Mercury. g) Absorption spectra of the films studied including amorphous rubrene.

of 100 nm amorphous rubrene films deposited on the TPTPA underlayer leading to their spherulitic form.

X-ray diffraction (XRD) is performed to identify the crystal structure of each crystalline film studied (Figure 1d). The XRD patterns consistent with rubrene in its orthorhombic crystal phase (space group Cmca) are obtained for the films corresponding to Figure 1a,b. A preferred orientation along the [100] axis is observed with an overall peak intensity stronger for the platelets compared to the spherulites, as expected from the higher degree of crystalline order within the single domain crystallites. Orthorhombic rubrene benefits from a herringbone packing (Figure 1e) leading to a large π-orbital overlap between molecules,[20] with preferred in-plane (bc-plane) charge transport.[14] The crystal phase adopted by the film in Figure 1c contains one peak near 12.5°, consistent with the rubrene triclinic (space group P-1) form (see the comparison of experimental XRD with simulated XRD patterns for the three polymorphs of rubrene in Figure S2, Supporting Information). The arrangement of molecular packing for triclinic rubrene, shown in Figure 1f, has less π-orbital overlap compared to the orthorhombic phase. We note that considering a triclinic film mainly oriented perpendicular to the [01-1] direction, the shorter stacking distance is situated in-plane.[21]

Absorption spectra of all samples studied in this work, including amorphous rubrene obtained without underlayer and annealing, are displayed in Figure 1g. As expected, we observe a relative decrease in the absorption peak ≈530 nm in orthorhombic rubrene.[22,23] The higher absorption of orthorhombic spherulites (compared to platelets) and triclinic spherulites (compared to amorphous) is likely due to the scattering of light as suggested by the visible roughness of the films. We note that absorption below 450 nm in all three crystalline samples is attributed to the TPTPA underlayer.[24]

This set of four films from fully amorphous to large grain (≈few 100s of μm) polycrystalline rubrenes with various crystal phases allows direct access to the interplay between order and charge transport while avoiding variations in the chemical nature of the molecule studied.

2.2. Thermally Activated Transport

We perform variable temperature current-voltage (I–V) measurements using a horizontal interdigitated architecture with a channel length of 150 μm. Ohmic contact (see Figure S3, Supporting Information) is achieved using MoO₃/Au electrodes. The conductivities extracted for one representative sample for each rubrene structure are displayed in **Figure 2**a (data of additional samples are given in Figure S4, Supporting Information). A four to five orders of magnitude increase in conductivity is observed between the amorphous and orthorhombic platelets samples at 300 K. As no electrical doping is involved in this study, this wide conductivity tuning range within one material highlights the importance of packing and π-orbital overlap on charge transport. The herringbone packing (Figure 1e) adopted by orthorhombic rubrene is particularly prone to large electronic couplings between molecules favoring charge transport.[20,25] This significant evolution in transport properties in rubrene, also observed in pentacene,[26,27] is reminiscent of the

decrease in carrier mobility by up to 6 orders of magnitude in amorphous silicon compared to its crystalline counterpart.[13]

We note that all samples exhibit a thermally activated transport with an increase in conductivity σ with increasing temperature. The activation energy E_A is extracted according to the Arrhenius law:

$$\sigma = \sigma_0 \exp\left(-E_A / k_B T\right) \tag{1}$$

with σ_0 is the conductivity prefactor, E_A the activation energy, k_B the Boltzmann constant and T the temperature. Details regarding the extraction of E_A with the formation of hysteresis in $\sigma - T$ for orthorhombic samples are provided in the Supporting Information (Figures S5 and S6, Supporting Information). We attribute the observed hysteresis and kink around 180 K in the $\sigma - T$ plot of orthorhombic rubrene samples to plastic deformation under thermal cycling. Conductivities (at 300 K) and activation energy values are summarized in **Table 1**.

Thermally activated hopping transport, described by the Gaussian disorder model (GDM, see Figure 2b(1)), is expected in amorphous OSCs, including rubrene, where the lack of order and weak intermolecular interaction favors localization of charges and incoherent hopping.[10,28,29] In disordered systems with a Gaussian density of states (DOS), an effective transport level E_t can be defined.[30] The activation energy E_A can be associated to the transition from the Fermi level E_F to E_t.[31] A similar conductivity magnitude and evolution is obtained in triclinic (spherulites) rubrene with activation energy slightly smaller than for amorphous rubrene. These results suggest that increased order through crystallization in the triclinic crystal phase is not sufficient to improve charge transport as triclinic rubrene adopts an unfavorable molecular packing for π-orbital overlap. A slightly narrower Gaussian DOS can be expected in the triclinic film from the small decrease in activation energy from amorphous to triclinic. A strong reduction in activation energy is obtained in orthorhombic rubrene films. While band-like transport is generally expected in rubrene single crystals from various experimental and theoretical results,[14–17,25,32,33] activation energy of ≈120 meV is extracted in polycrystalline (orthorhombic platelets) rubrene films. Considering that transport is not significantly disrupted within the crystallites of rubrene, thermal activation of conductivity may be due to energy barriers at grain boundaries or associated with the mobility edge model (or multiple trapping and thermal release model). Energy barriers at grain boundaries (Figure 2b(2)) are for example attributed to thermally activated transport in polycrystalline silicon and other polycrystalline materials.[12,34,35] The mobility edge model as illustrated in Figure 2b(3) is commonly used to describe transport in amorphous silicon where a mobility edge separates extended bands from discrete energy levels forming exponential tail states where carriers are localized.[36] Therefore, carriers can coherently travel following band-like transport after being thermally activated from the tail states with an activation energy E_A. With decreasing temperature, the transport mechanism may transition to variable range hopping (VRH), as the probability for thermal release becomes too small.[36] In the case of the VRH model and the GDM, the Arrhenius law (Equation (1)) must be slightly modified.[12,31]
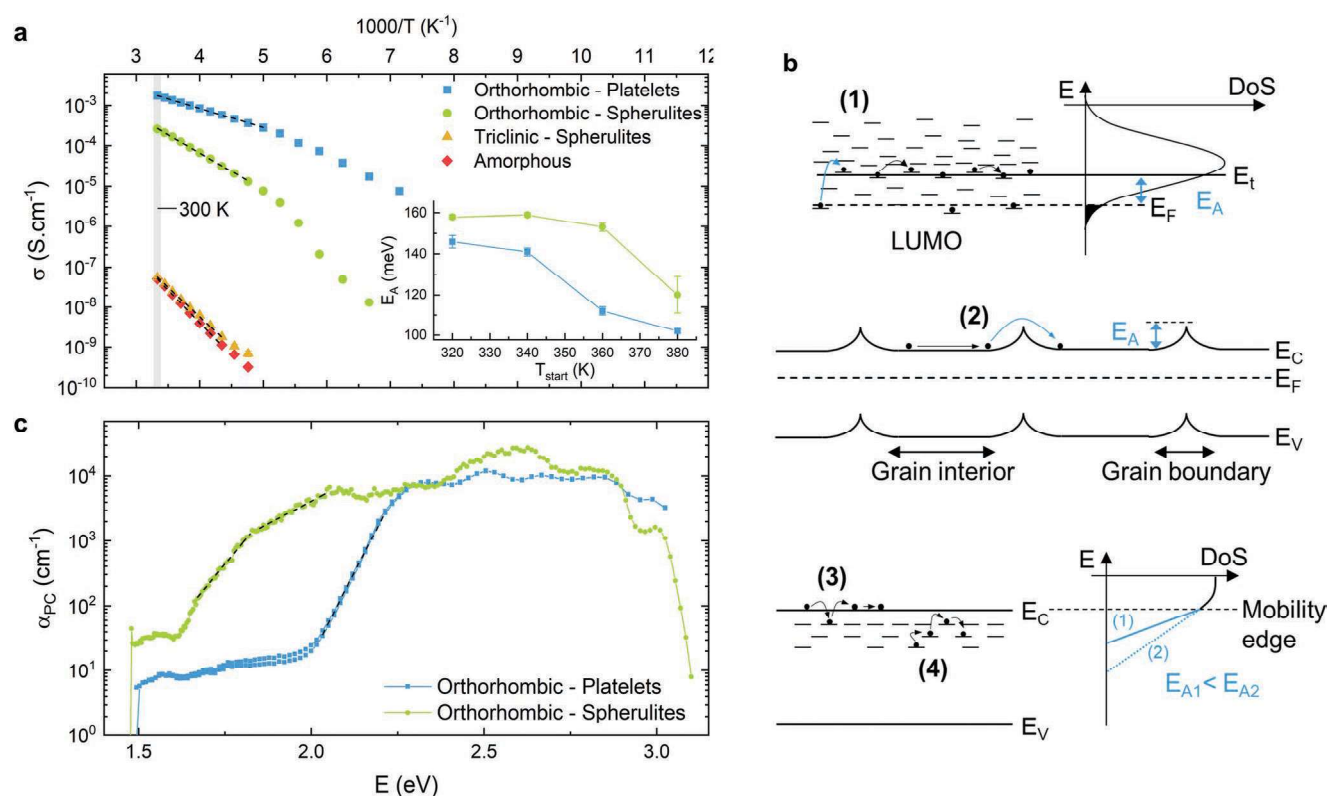
Figure 2. a) Variable temperature conductivity for rubrene in its orthorhombic platelets, orthorhombic spherulites, triclinic spherulites, and amorphous forms. The exponential (linear in semi-log) fits for the activation energy E_A extraction (given in Table 1) are shown in dashed lines. The inset shows the evolution of E_A for one orthorhombic platelet and one orthorhombic spherulite sample as a function of the starting temperature of the measurement (i.e., the highest temperature the sample has been exposed to before conductivity measurements and E_A extraction). b) Schematic representation of various transport models developed to describe charge transport (here for electrons in the conduction band/LUMO) in ordered and disordered semiconductors: 1) Gaussian disorder model for hopping transport with an effective transport level E_t (the activation energy E_A is given by the difference between the Fermi level E_F and E_t); 2) Grain boundary energy barriers E_A; 3) Multiple trap and release model (or mobility edge model) with μ_{edge} corresponding to the mobility edge and E_{A1} and E_{A2} the activation energies depending on the extent of the tails states; 4) Variable range hopping (VRH) model. c) Absorption coefficient calculated from photoconductivity spectra for orthorhombic platelets and spherulite samples. The Urbach energies E_U are extracted with the exponential fit (linear in semi-log) in dashed lines.

In order to determine whether thermal activation for transport in orthorhombic rubrene is associated with energy barriers at grain boundaries, or due to intrinsic properties of the OSCs potentially illustrated by the mobility edge model, we perform photoconductivity spectroscopy to extract the Urbach energy E_U. The Urbach energy corresponds to the exponential absorption tail and contains both thermal and structural disorder components.[37] While E_U is normally extracted from the absorption coefficient, photoconductivity measurements offer a higher sensitivity to probe tail states and other sub-bandgap features than common absorption spectroscopy setups.[38,39] Assuming that the photoconductivity spectrum is dominated by absorption (i.e., electrical properties are wavelength independent), it is possible to deduce the absorption coefficient from photoconductivity α_{PC} and extract E_U (additional details on α_{PC} calculation in Figure S7, Supporting Information).[40,41] We note that, while most OSCs do not exhibit a photocurrent on their own due to the high exciton binding energy, the conductivity of crystalline rubrene is shown to increase with light intensity and is attributed to exciton dissociation at the

Table 1. Summary of the values extracted throughout this study and averaged over 2 to 3 samples: dark conductivity at 300 K σ_{dark} the activation energy for transport E_A, Urbach energy E_U, hole density p_{dark}, and mobility $\mu_{p,dark}$ the dark mobility from Hall effect measurements (note: only values for samples exhibiting a clear predominant band-like transport are given in this table), magnetoresistance MR, and the Gaussian standard deviation σ_G calculated from E_A using Equation (7).

Crystal phase – Morphology	σ_{dark} @ 300 K [S cm^{-1}]	E_A [meV]	E_U [meV]	p_{dark} [cm^{-3}]	$\mu_{p,dark}$ [cm^{2}V^{-1}s^{-1}]	MR [%]	σ_G from E_A [meV]
Orthorhombic – Platelets	$(1.1 \pm 0.9) \times 10^{-3}$	120 ± 40	30 ± 10	$(8 \pm 2) \times 10^{14}$	2 ± 1	–	60 ± 20
Orthorhombic – Spherulites	$(2.0 \pm 0.6) \times 10^{-4}$	160 ± 30	$70 \pm 10/155 \pm 15$	–	–	0.005 ± 0.1	70 ± 10
Triclinic – Spherulites	$(4 \pm 3) \times 10^{-8}$	300 ± 10	–	–	–	0.11 ± 0.03	94 ± 3
Amorphous	$(6 \pm 1) \times 10^{-8}$	330 ± 5	–	–	–	0.23 ± 0.08	98 ± 1

**ADVANCED
SCIENCE NEWS**
www.advancedsciencenews.com

**ADVANCED
FUNCTIONAL
MATERIALS**
www.afm-journal.de

crystal surface.[42–44] With an exciton diffusion length estimated at 3 − 8 µm in rubrene single crystals,[42] exciton dissociation and creation of photocurrent can be expected in polycrystalline films of 100 nm in thickness.

Figure 2c displays the calculated α_{PC} spectra for orthorhombic rubrene in both platelet and spherulitic forms (the photoconductivity is too low for triclinic and amorphous rubrene). In the orthorhombic platelet sample, an abrupt tail is observed with a corresponding E_U of ≈30 meV, consistent with values extracted in rubrene single crystals using other methods.[45,46] As absorption integrates transitions from the HOMO tail to the LUMO tail, we expect E_U to be larger than the energy of the HOMO tail alone probed by conductivity measurements. With activation energy at ≈120 meV for orthorhombic platelet rubrene, we can conclude that the degree of disorder (static and dynamic) within the grains is not responsible for the thermally activated transport. As a consequence, we believe that grain boundaries are responsible for the thermally activated transport and attribute the activation energy E_A to the energy barrier at grain boundaries. This observation is consistent with the increase in conductivity observed with grain size (see the comparison between samples 1 and 2 in Figure S4a, Supporting Information). As an alternative to energy barriers, the formation of tail states at grain boundaries could also account for thermal activation through the mobility edge model for spatially localized defects.[47]

The transport mechanism involved in orthorhombic spherulite samples is less clearly identified. The photoconductivity exhibits a strong sub-bandgap contribution and two E_U values can be extracted from α_{PC} spectra (Figure 2c and Table 1). While the largest E_U value of ≈155 meV is close to the activation energy of ≈160 meV, potentially pointing toward the mobility edge model, a second and steeper slope is observed with a corresponding E_U of ≈70 meV. Overall, the broad tail suggests a strong increase in static disorder in the spherulitic samples and is associated with the crystal orientation misalignment within the grains. Additionally, grain boundaries in spherulitic films of orthorhombic rubrene have been shown to suffer from a higher degree of molecular misalignment compared to the platelet morphology,[48] which could also explain an increase in activation energy and decrease in conductivity. We note that activation energy for transport can be reduced by exposing the sample to increasing temperature for both the orthorhombic platelets and spherulite samples (inset of Figure 2a). The heat exposure likely heals defects at grain boundaries and may help reduce disorder-induced tail states in spherulitic samples.

2.3. Ultra-Sensitive AC Hall and Magnetoresistance Measurements

In order to deepen our understanding of transport properties in rubrene with varying order and morphology, we perform photo-Hall and magnetoresistance measurements on rubrene films using an ultra-sensitive ac Hall setup based on a rotating parallel dipole line (PDL) magnet Hall system.[49,50] The PDL Hall system enables the generation of pure single harmonic magnetic field oscillations allowing for Hall and magnetoresistance measurements in highly resistive samples. The ability to probe

the Hall effect in OSC films without the need for "gating" (i.e., formation of an accumulation layer with the help of a gate bias) provides access to intrinsic properties of the semiconductors without interference from additional carriers (either through gate bias or electrical doping) or defects and scattering at the dielectric/semiconductor interface.[51]

Figure 3a displays the Hall density (n_{Hall} or p_{Hall}) and resistance R_H measured for each rubrene crystal phase and morphology as a function of absorbed photon density G_γ (details about the calculation of G_γ are given in ref. [52]). As illustrated in Figure 3b for an orthorhombic spherulite rubrene sample, the transverse resistance R_{xy} is measured, and R_H is obtained from Fourier transform and lock-in detection on the magnetic field (additional details on R_H extraction in Figures S8 to S11, Supporting Information). In the dark, R_H is related to the carrier density n_{Hall} for electron (or p_{Hall} for hole) according to the equation:

$$\frac{dR_H}{B} = \pm \frac{1}{q n_{Hall}} \tag{2}$$

with d the semiconductor thickness, B the magnetic field, and q the elementary charge. The sign of the measured Hall signal indicates the majority charge carrier (positive for holes and negative for electrons). In the case of rubrene, we expect equation (2) to remain valid under illumination due to hole-only conduction in the material (electrons are trapped and $\mu_n \ll \mu_p$ with μ_n and μ_p the electron and hole mobilities).[53,54] For orthorhombic rubrene with platelet morphologies, a positive Hall signal is detected and a carrier density of $p_{Hall} \approx 10^{15}$ cm^{-3} is extracted, consistent with values expected in OSCs. An increase of p_{Hall} (decrease of R_H) with increasing light intensity is observed confirming the photogeneration of carriers. A value of ≈ 2 cm^2 V^{-1} s^{-1} is obtained for the hole mobility $\mu_{Hall} = \sigma/q p_{Hall}$, consistent with values measured in a polycrystalline rubrene field effect transistor (FET) with similar morphology.[55–57] The decrease in mobility by one order of magnitude compared to typical values measured in rubrene single crystals (measured with FET or Hall with gate bias),[15,45,51] is consistent with the hypothesis of grain boundary-limited carrier transport in polycrystalline orthorhombic platelets films, and as observed in polycrystalline compared to single crystalline silicon.[12,34]

While we do not expect a change in carrier density with crystal phase and morphology, a strong increase in R_H is observed as we move toward orthorhombic spherulites, triclinic spherulites, and amorphous rubrene. We highlight that, while we are confident a Hall signal is probed for these highly resistive samples (see Figure S12, Supporting Information) with a clear trend with increasing disorder, the exact value of R_H must be taken with care as we approach the limit of the equipment sensitivity of measuring resistance larger than ≈100 GΩ. For amorphous rubrene, a Hall density (positive) of ≈10⁹ cm^{-3} and slightly increasing with illumination is extracted. The strong deviation of the Hall density from the expected carrier density suggests a decreased contribution of band-like transport as only coherently traveling carriers are sensitive to the Lorentz force involved in the Hall effect.[58,59] Hall measurements are therefore a valuable tool to probe the degree of disorder in a
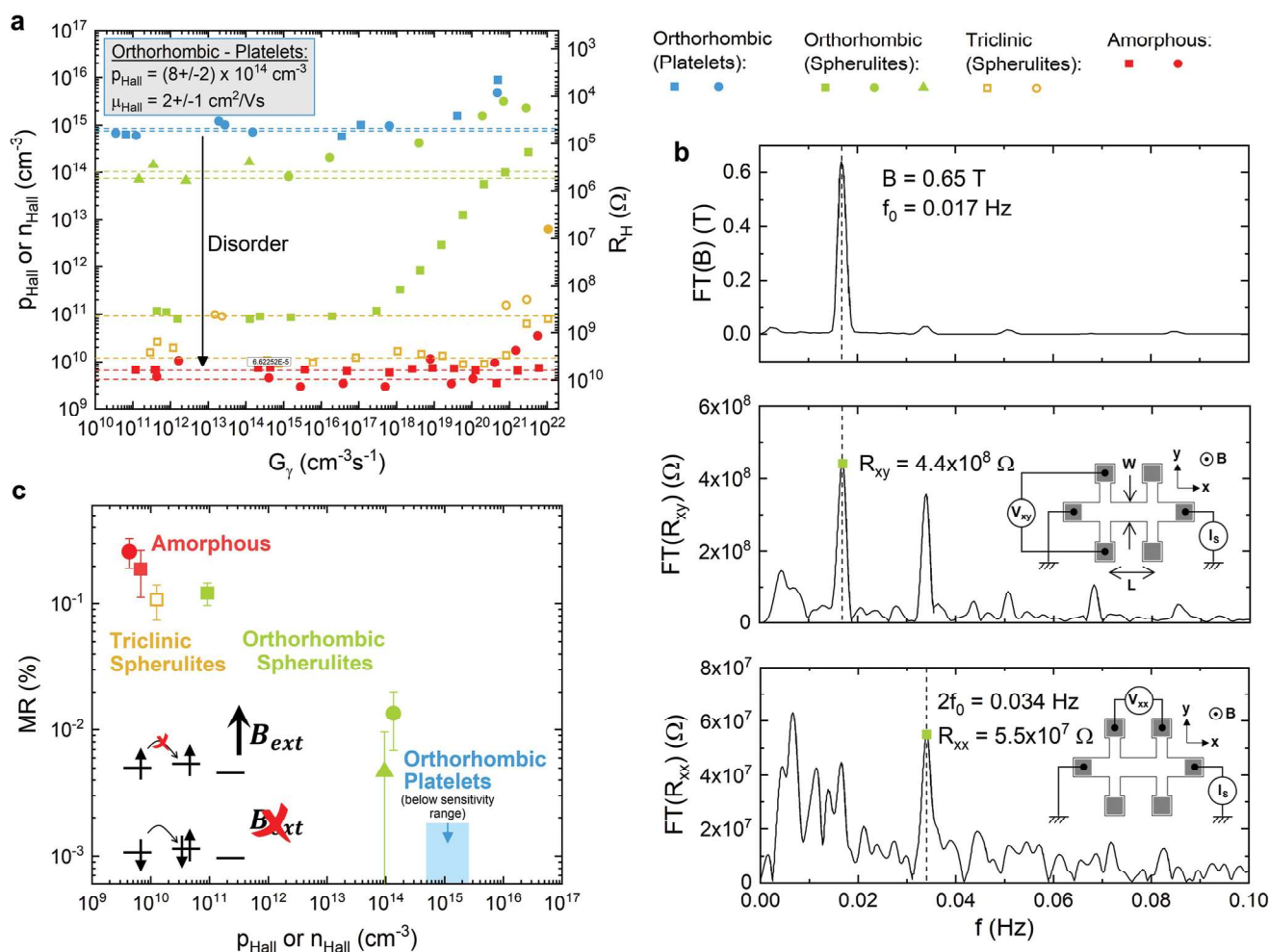
ADVANCED
SCIENCE NEWS
www.advancedsciencenews.com

ADVANCED
FUNCTIONAL
MATERIALS
www.afm-journal.de

Figure 3. a) Hall density p_{Hall} or n_{Hall} and Hall resistance R_H measured for various samples of orthorhombic platelets, orthorhombic spherulites, triclinic spherulites, and amorphous rubrene. Solid symbols exhibit a positive Hall signal (leading to an extracted p_{Hall}) and open symbols exhibit a negative Hall signal (leading to an extracted n_{Hall}). The Hall data are given as a function of absorbed photon density G_γ at $\lambda \approx 500$ nm . b) Fourier transform of the magnetic field signal B, transverse resistance R_{xy} and longitudinal resistance R_{xx} extracted in an orthorhombic spherulitic sample of rubrene in the dark (additional details and extractions for other samples in Figures S8 to S11, Supporting Information). The insets in the middle and bottom panels show schematics of transverse V_{xy} and longitudinal V_{xx} voltage extraction upon application of a current source I_S and magnetic field B. A channel length and width of 4 and 2 mm are used for the Hall bar. c) Magnetoresistance MR values for each sample are plotted as a function of p_{Hall} or n_{Hall}. All magnetoresistance values are positive. Solid and open symbols correspond to positive and negative R_H, respectively. No magnetoresistance was observed in orthorhombic platelet samples. A schematic of spin blocking upon magnetic field exposure associated with the bipolaron model is given as an inset.

semiconductor.[60,61] We also note that, according to a model developed by Yi et al.,[58] $n_{Hall} \ll n$ with n the carrier density is expected for $\mu_{hopping} \ll \mu_{band}$ and $n_{band} \ll n$, with $\mu_{hopping}$, μ_{band} and n_{band} the hopping mobility, band mobility and band density, respectively. Therefore, our measurement on amorphous rubrene (see Figure S11, Supporting Information) suggests that a Hall signal can be probed even in a situation with predominant hopping transport, provided a sufficient sensitivity of the measurement setup. It is worth recalling that the association of the Hall signal with band-like transport in a semiconductor must be done with care, and further evidence must be provided to support the predominance of this transport mechanism over hopping.[58] As an example, the extracted density and/or mobility values may be compared with values obtained (or reported) using alternative characterization techniques (such as concomitant FET measurements).[15,62,63] A

similar underestimation of the Hall density is obtained in triclinic rubrene with, however, a negative sign. Interestingly, a sign anomaly has also been observed in amorphous silicon and associated with hopping transport.[64,65] Further work is required to better understand the Hall effect in materials with strong hopping contributions.

The behavior of orthorhombic rubrene with spherulitic morphology is of particular interest with a range of p_{Hall} (positive R_H) spanning over 3 orders of magnitude for various samples. In spherulitic samples, the disorder induced by the gradient in crystalline orientation within the grains may be sufficient to reach the threshold between localized and delocalized charge carrier transport. At the limit between band-like and hopping charge transport, the value of p_{Hall} (or R_H) is strongly dependent on the level of order within the spherulitic films, which may vary between samples. It is interesting to note that p_{Hall}

**ADVANCED
SCIENCE NEWS**

www.advancedsciencenews.com

**ADVANCED
FUNCTIONAL
MATERIALS**

www.afm-journal.de

increases more rapidly than conductivity under illumination for the orthorhombic spherulite sample with the lowest p_{Hall} (i.e., lowest band-like transport contribution, see Figure S13, Supporting Information), and eventually reaches values closer to orthorhombic platelet samples. Overall, these results suggest a gradual transition from hopping (incoherent) toward band-like (coherent) transport under illumination, as previously observed in polycrystalline OSCs with increasing gate bias or doping concentration.[28,66–68] Extra carriers added through photogeneration (illumination) or formation of an accumulation layer (gate bias) may progressively fill localized tail states allowing access to the extended band.

In addition to the Hall effect, magnetoresistance measurements are performed using the same PDL Hall system with the extraction of the longitudinal resistance R_{xx}. Organic magnetoresistance (OMAR) is observed mostly in disordered OSCs where hopping transport is predominant.[69,70] In particular, OMAR effects have been reported in the background signal of amorphous rubrene-based spin valve devices.[71] The magnetoresistance follows a quadratic function of B and is therefore visible at the second harmonic in the Fourier transform (Figure 3b lower panel).[70] Due to the finite size of the Hall bar, R_{xx}-R_{xy} mixing may lead to magnetoresistance and Hall contributions in the transverse and longitudinal signals, respectively.[52] From the determination of R_{xx}, we can deduce the magnetoresistance MR defined by:

$$MR = \frac{R(B) - R(0)}{R(0)} = \frac{R_{xx}}{R(0)} \tag{3}$$

with $R(0)$ the background resistance without a magnetic field.[69] While no R_{xx} signal is probed in orthorhombic platelet rubrene, MR values are extracted for all other rubrene structures and summarized in Figure 3c. The observation of a dark magnetoresistance leads us to attribute this signal to the bipolaron model.[70] The magnetic field prevents spin mixing and therefore the formation of bipolarons, disrupting transport and leading to a positive magnetoresistance (schematic as an inset in Figure 3c).[72] The absence of magnetoresistance signal in orthorhombic platelet rubrene is therefore consistent with band-like transport.[69] The OMAR magnitude is expected to increase with the degree of disorder in the film as more sites become favorable for bipolaron formation.[69,70,72] The correlation observed between MR and p_{Hall} or n_{Hall} shown in Figure 3c is fully consistent with an increase in disorder when moving toward amorphous rubrene. The observation of OMAR with variable intensity in orthorhombic spherulite samples confirms the transition from band-like transport toward the formation of localized polarons and bipolarons and the coexistence of both transport mechanisms in the film. In an effort to continue the parallel between rubrene and silicon, we note that magnetoresistance has been measured in amorphous silicon and attributed to hopping on localized states.[73]

3. Discussion

In the context of varying hopping and band-like contributions for a given OSC, we try to understand the meaning of the Hall mobility μ_{Hall} and conductivity prefactor σ_0 from the Arrhenius law (Equation (1)). If we consider a total carrier density $p \approx 10^{15}$ cm^{-3} identical for all rubrene samples, we can calculate a mobility prefactor $\mu_0 = \sigma_0 / qp$. While the conductivity spans over 5 orders of magnitude between amorphous and crystalline rubrene, μ_0 remains relatively constant spreading within 2 orders of magnitude and centered $\approx$ 100 cm^{2}V^{-1}s^{-1} (**Figure 4**a). The mobility prefactor exceeds the expected band mobility of rubrene by approximately one order of magnitude, a behavior previously observed in various OSCs.[74] In addition, we can compare μ_0 to the Hall mobility μ_{Hall} calculated from p_{Hall} and σ measured at ambient temperature. If we consider the conductivity to be a superposition of the hopping σ_{hop} and band-like σ_{band} contributions $\sigma = \sigma_{\text{hop}} + \sigma_{\text{band}}$, μ_{Hall} is related to the band-like mobility μ_{band} by: [58]

$$\mu_{\text{Hall}} = \mu_{\text{band}} \frac{\gamma}{\gamma - \gamma\beta + \beta} \tag{4}$$

with $\gamma = p_{\text{band}} / p$ the fraction of band-like carriers p_{band}, and $\beta = \mu_{\text{hop}} / \mu_{\text{band}}$ the ratio of hopping and band-like mobilities. If $\gamma \gg \beta$, equation (4) simplifies to $\mu_{\text{Hall}} \sim \mu_{\text{band}}$. While we do not have access to the value of γ, we can expect $\beta \approx 10^{-6} - 10^{-7}$ in rubrene.[75,76] For amorphous and triclinic rubrene we obtain $\mu_{\text{Hall}} \sim \mu_0$, suggesting a common origin. We note that μ_{Hall} is smaller for orthorhombic platelets as energy barriers at grain boundaries limit the effective mobility in the film. Orthorhombic spherulite rubrene marks a transition between predominant band-like and predominant hopping transport as suggested from previous measurements.

Our experimental results point toward a common transport model for rubrene in various crystalline forms with a varying contribution of band-like (delocalized) and hopping (localized) carriers. The contribution of band-like transport likely depends on the fraction of band-like carriers γ. If we consider a simple model where the HOMO DOS is described by a Gaussian distribution $g(E)$:

$$g(E) = \frac{N_V}{\sqrt{2\pi}\sigma_G} \exp\left(-\frac{E^2}{2\sigma_G^2}\right) \tag{5}$$

with E the energy, N_V the effective density of states and σ_G the standard deviation of the Gaussian distribution representative of energetic disorder, the ratio γ is given by:

$$\gamma = \frac{p_{\text{band}}}{p} = \frac{\int_{-BW/2}^{BW/2} f(E) g(E) dE}{\int_{-\infty}^{+\infty} f(E) g(E) dE} \tag{6}$$

where $f(E)$ is the Fermi-Dirac distribution and BW is the bandwidth determined by the intermolecular coupling (π-orbital overlap). As illustrated in Figure 4b, transport of carriers in the extended states at the center of the Gaussian distribution (within the bandwidth) is coherent, while incoherent transport occurs for carriers situated deeper in the Gaussian tail on the localized states. We note that, in the Gaussian DOS model, the parameter σ_G is related to the activation energy for thermal transport E_A according to:[29]
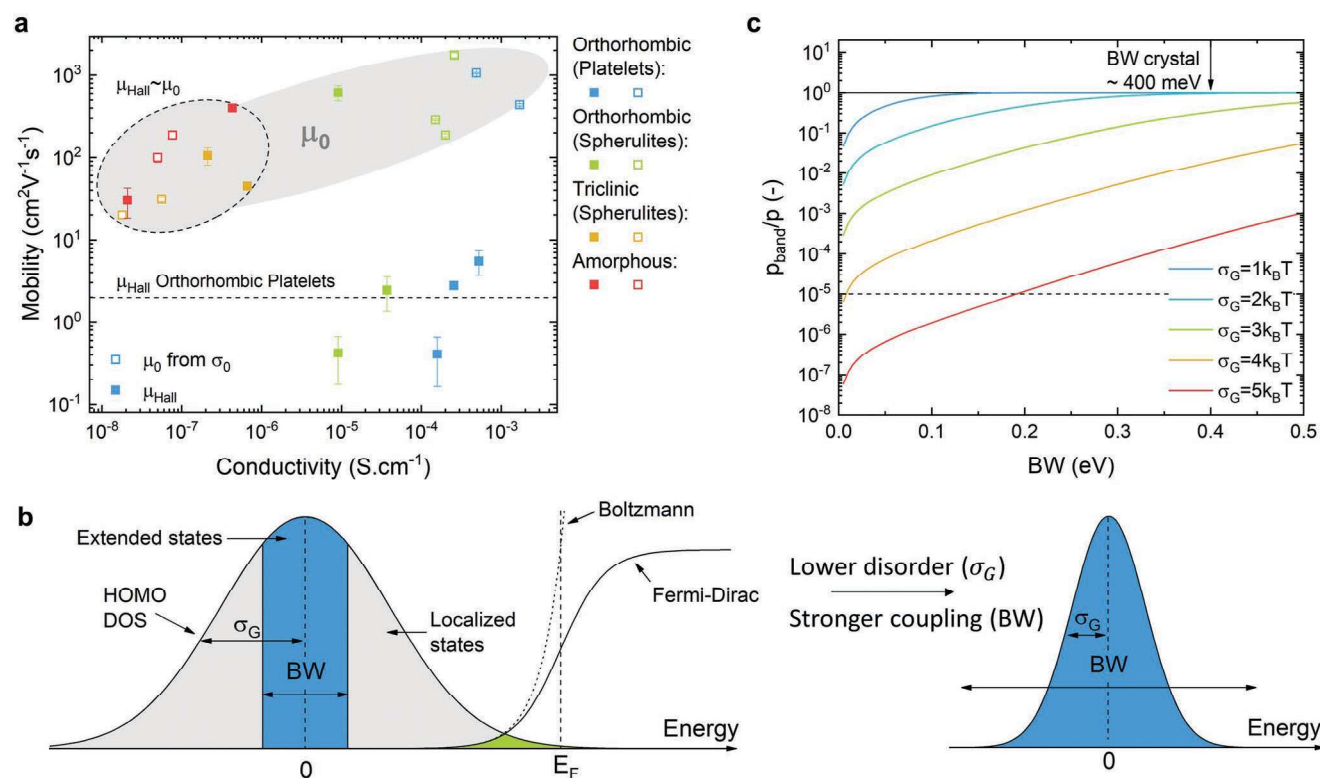
$$E_A = \frac{8}{9} \frac{\sigma_G^2}{k_B T}. \tag{7}$$

Figure 4. a) Mobility μ_0 (open symbols) calculated from the conductivity prefactor σ_0 in Equation (1 considering a carrier density of 10^{15} cm^{-3}, and Hall mobility μ_{Hall} (solid symbols) as a function of sample conductivity at 300 K. b) Schematic representation of a Gaussian DOS for the HOMO level, the Fermi-Dirac distribution and Boltzmann approximation positioned at the Fermi level E_F. BW and σ_G correspond to the bandwidth and Gaussian standard deviation, respectively. States are extended within the BW (blue area) and localized further away from the center of the Gaussian distribution (grey area). The green area corresponds to the superposition of the Boltzmann function and the HOMO DOS. (c) Ratio p_{band}/p_{total} as a function of BW calculated analytically for σ_G varying between $1k_BT$ and $5k_BT$. p_{band} corresponds to the density of carriers within the BW and p corresponds to the total density of carriers.

Calculated values of σ_G considering the activation energies extracted from variable temperature conductivity measurements are summarized in Table 1. We also highlight that, in the framework of pure Gaussian DOS without exponential tails, the Urbach energy E_U (extracted in Figure 2c) is more directly related to σ_G than the activation energy E_A.[11] In the low carrier density regime, we can approximate the Fermi-Dirac distribution considering the Boltzmann approximation, allowing for equation (6) to be solved analytically and leading to:

$$\gamma = -\frac{1}{2}\left[Erf\left(\frac{\sigma_G^2 - \frac{BW}{2}k_BT}{\sqrt{2}\sigma_G k_BT} \right) - Erf\left(\frac{\sigma_G^2 + \frac{BW}{2}k_BT}{\sqrt{2}\sigma_G k_BT} \right) \right] \quad (8)$$

where Erf corresponds to the error function. Figure 4c displays $\gamma = p_{Hall}/p$ as a function of BW for various σ_G ranging from 1 to $5k_BT$. As expected, γ approaches unity (i.e., all carriers are band-like) when σ_G decreases (i.e., disorder is minimized), and BW increases (i.e., intermolecular coupling increases). Crystalline rubrene (in the orthorhombic crystal phase) is notable for a relatively strong intermolecular coupling leading to a BW estimated and measured ≈ 400 meV,[17,32] and responsible for its band-like transport mechanism as suggested by Figure 4c for $\sigma_G \approx 50$ meV ($\approx 2k_BT$) expected in crystalline rubrene.[77,78]

The higher values of σ_G calculated from E_A (see Table 1) are consistent with the contribution of grain boundaries in the activation energy for thermal transport for orthorhombic platelet rubrene. As disorder increases, σ_G approaches values $\approx 4k_BT$ calculated from E_A (Table 1) and consistent with values expected for amorphous OSCs.[77] If we consider that $p_{band} \sim p_{Hall}$, we can estimate $\gamma \sim 10^{-5}$ in amorphous rubrene, therefore leading to a $BW \approx 10$ meV. While this remains only a rough estimate given the uncertainty in R_H extraction of high resistivity samples, combined with approximation of the true DOS by a Gaussian distribution, we note that delocalization over two molecules is expected in rubrene for a transfer integral $t \approx 10$ meV (corresponding to $BW = 4t \approx 40$ meV).[61] As transport transitions from fully incoherent (i.e., $p_{band} \approx 0$) to partially coherent when carriers become delocalized over a few molecules,[60,61] we can expect amorphous rubrene to be at the edge of a fully incoherent transport. While a transport mechanism termed transient localization has been developed to account for the apparent coexistence of delocalized and localized carriers in crystalline OSCs,[79,80] the origin of this coexistence in semicrystalline and amorphous OSCs with delocalization of fewer than two molecules remains marginally explored.[81]

Our experiments support that order and intermolecular coupling are paramount for optimized transport properties.[82] As rubrene evolves from an ideal orthorhombic phase with

ADVANCED
SCIENCE NEWS
www.advancedsciencenews.com

ADVANCED
FUNCTIONAL
MATERIALS
www.afm-journal.de

herringbone packing allowing for strong intermolecular interactions to an amorphous phase, the Gaussian DOS widens due to increased energetic disorder. Most importantly, as intermolecular interactions are expected to decrease exponentially with intermolecular distance,[9] the *BW* drops dramatically in amorphous rubrene. Additionally, the intermolecular coupling is highly dependent on orbital overlap defined not only by distance but also by molecular packing. While triclinic and orthorhombic polymorphs of rubrene possess the same molecular density and intermolecular stacking distance ($\approx$3.73 Å), the orbital overlap between molecules is not optimized in the triclinic crystal phase.[21,83] In the case of triclinic rubrene, we can therefore expect a lower energetic disorder (lower σ_G) suggested by its crystalline arrangement, accompanied by weaker intermolecular interactions (lower *BW*) than in randomly oriented amorphous rubrene films.

The observed predominance of packing over the order in our study is in agreement with the high mobilities achieved in polycrystalline and even amorphous OSCs through the engineering of side chains to improve packing and molecular orbitals to increase overlap.[9,84–86] Additionally, molecules can be functionalized to optimize orbital overlap in the crystalline arrangement.[87,88] We can therefore infer that molecular design favoring strong intermolecular interaction is likely the most efficient strategy to improve transport properties in OSCs. Additionally, the emerging class of materials of 2D covalent organic frameworks (2D-COFs) shows great promise for efficient transport with access to highly ordered structures with molecular packing ideal for charge transport and inaccessible in traditional OSCs.[89–91] Through the appropriate design of organic molecules, we may achieve the carrier mobilities required for high switching speed transistors.[92,93] Larger exciton and carrier diffusion lengths are also of particular interest for solar cells and photodetectors.[94]

4. Conclusion

To conclude, we reported a comprehensive study of the interplay between molecular packing and charge transport properties without variations in the chemical nature of the molecule. The results obtained on rubrene are consistently compared to previous knowledge acquired on amorphous, polycrystalline, and single crystalline silicon, highlighting similarities between two families of materials often emphasized by their differences. We show that, similar to silicon, structural order can have a significant impact on transport in rubrene, changing the conductivity over orders of magnitude and modifying the transport mechanisms from band-like in orthorhombic polycrystalline rubrene to hopping in its amorphous phase. However, our study highlights that order is not sufficient and intermolecular coupling is paramount for optimal transport properties. While covalent bonds in crystalline silicon ensure efficient transport, OSCs suffer from weak intermolecular forces and the design of molecules should allow for ideal molecular packing reducing intermolecular distance and advantageous π-orbital overlap. Our results point toward the application of a common transport model with varying contributions of delocalized and localized carriers associated with order and packing. Relying on a

deeper understanding of the underlying mechanisms controlling transport in organic semiconductors, our study provides specific guidelines for the design of more efficient materials for organic electronics.

5. Experimental Section

Device Fabrication: Rubrene and TPTPA were purchased from Lumtec and rubrene was purified by thermal gradient sublimation prior to evaporation. Rubrene films were grown on glass substrates cleaned through successive sonication at 45 °C in deionized water, acetone, and isopropanol for 15 min each, followed by a 10 min oxygen plasma treatment. Amorphous rubrene films were obtained by evaporating (using an Angstrom Engineering evaporator operating at a base pressure $\approx$10^{-6} Torr) 100 nm of rubrene directly on glass. For crystalline rubrene films, a 5 nm thick TPTPA underlayer was evaporated prior to rubrene deposition. Triclinic rubrene samples were obtained with a subsequent 100 nm rubrene film and annealed at 145 °C for 10 min. Orthorhombic rubrene films (both platelets and spherulites) were processed through a two-step deposition method. A 20 nm crystalline template layer was first grown with an annealing step of 145 °C-10 min to obtain platelets and 155 °C-3 min to obtain spherulites on 1 × 1 cm substrates (used for variable temperature *I–V* measurements). 3 × 3 cm substrates used for Hall, magnetoresistance, and photoconductivity measurements require an annealing step of 10 min at 152 °C to reach platelet films with full coverage (no change in annealing temperature for spherulites). Homoepitaxy was subsequently performed with a substrate temperature of 80 °C and a deposition rate of 0.5 Å s^{-1} to reach the desired thickness of 100 nm. MoO$_3$ (5 nm)/Au (100 nm) electrodes were evaporated through a shadow mask. Hall devices were encapsulated with glass using epoxy glue deposited on the perimeter. Device fabrication was performed in a nitrogen-filled glovebox with oxygen and water levels below 0.1 ppm.

Structural and Optical Characterization: POM images were taken with an Olympus BX60F5, XRD spectra were measured using a Bruker D8 Discover X-ray Diffractometer, UV–visible absorption spectroscopy was performed with a UV-vis Cary 5000 Spectrophotometer, and AFM images were obtained with a Veeco Innova.

Variable Temperature I–V measurements: Samples were transferred from the glovebox to an ultra-high vacuum (base pressure $\approx$10^{-8} Torr) for *I–V* measurements without exposure to air. Temperature was varied between 100 K and 300 K (380 K for high-temperature measurements) using a closed-cycle He refrigerator combined with a heater. *I–V* measurements was carried out using a Keithley 2400 source meter.

Hall and Magnetoresistance and Photoconductivity Measurements: A parallel dipole line (PDL) Hall system was used to generate a unidirectional and pure single harmonic ac magnetic field monitored by a Hall sensor. The sample was mounted at the center of the PDL system where a magnetic field amplitude of 0.65 T was obtained. A detailed description of the PDL Hall system and its photo-Hall optics have been described in Ref. ([49]), ([50]), and ([52]). Light illumination using supercontinuum laser SuperK Fianium FIU-15 from NKT Photonics was used as the light source. The wavelength could be tuned from 400 to 840 nm using SuperK VARIA tunable filter and the light intensity could be modulated over eight orders of magnitude using continuous neutral density filters. A wedge lens was used to deflect the light beam onto the sample. A beam splitter was used to simultaneously illuminate the sample and a silicon photodetector to monitor the photocurrent at various light intensities and determine the incident-absorbed photon density on the sample. A Keithley 2450 Source Meter Unit (SMU) was used to apply the current source and a Keithley 2001 Digital Multi Meter (DMM) for voltage measurement. A Keithley 7065 Hall switch matrix card with high impedance buffer amplifiers was used for routing the signals between the samples, the SMU and DMM. The current of the silicon photo-detector was monitored using a Keithley 617 electrometer. Applied bias voltage of 10 V across the six

terminal Hall bar device was used. The analysis of the Hall signal over time was performed using a custom-developed software developed in Matlab.[50] A Fourier spectral analysis was performed on the transverse (Hall) and longitudinal (magnetoresistance) resistance after polynomial background subtraction to identify the Hall signal of the same frequency with the reference oscillating magnetic field, and the magnetoresistance signal at the second harmonic. Finally, software lock-in detection was performed to extract the final Hall and magnetoresistance values from the raw resistance traces. A typical lock-in time constant of 120 s. was used Additional information on the photo-Hall setup and data analysis could be found elsewhere.[52] Photoconductivity data were obtained from longitudinal resistance measurements without an applied magnetic field.

Supporting Information

Supporting Information is available from the Wiley Online Library or from the author.

Conflict of Interest

The authors declare no conflict of interest.

Data Availability Statement

The data that support the findings of this study are available from the corresponding author upon reasonable request.

[1] H. Shirakawa, E. J. Louis, A. G. Macdiarmid, C. K. Chiang, A. J. Heeger, J. Chem. Soc., Chem. Commun. 1977, 16, 578.
[2] C. J. Brabec, Sol. Energy Mater. Sol. Cells 2004, 83, 273.
[3] N. Thejo Kalyani, S. J. Dhoble, Renew Sustain Energy Rev 2012, 16, 2696.
[4] B. Geffroy, P. le Roy, C. Prat, Polym. Int. 2006, 55, 572.
[5] H. Klauk, Chem. Soc. Rev. 2010, 39, 2643.
[6] A. C. Arias, J. D. MacKenzie, I. McCulloch, J. Rivnay, A. Salleo, Chem. Rev. 2010, 110, 3.
[7] G. Hong, X. Gan, C. Leonhardt, Z. Zhang, J. Seibert, J. M. Busch, S. Bräse, Adv. Mater. 2021, 33, 2005630.
[8] P. Hu, X. He, H. Jiang, InfoMat 2021, 3, 613.
[9] H. Sirringhaus, T. Sakanoue, J. F. Chang, Phys. Status Solidi Basic Res. 2012, 249, 1655.
[10] V. Coropceanu, J. Cornil, D. A. da Silva Filho, Y. Olivier, R. Silbey, J.-L. Bredas, Chem. Rev. 2007, 107, 926.
[11] S. Fratini, M. Nikolka, A. Salleo, G. Schweicher, H. Sirringhaus, Nat. Mater. 2020, 19, 491.
[12] L. P. Scheller, N. H. Nickel, J. Appl. Phys. 2012, 112, 013713.
[13] A. R. Moore, Appl. Phys. Lett. 1977, 31, 762.
[14] V. Podzorov, E. Menard, A. Borissov, V. Kiryukhin, J. A. Rogers, M. E. Gershenson, Phys. Rev. Lett. 2004, 93, 086602.
[15] V. Podzorov, E. Menard, J. A. Rogers, M. E. Gershenson, Phys. Rev. Lett. 2005, 95, 226601.
[16] J. Takeya, K. Tsukagoshi, Y. Aoyagi, T. Takenobu, Y. Iwasa, Jpn. J. Appl. Phys. 2005, 44, L1393.
[17] S. I. MachHida, Y. Nakayama, S. Duhm, Q. Xin, A. Funakoshi, N. Ogawa, S. Kera, N. Ueno, H. Ishii, Phys. Rev. Lett. 2010, 104, 14.
[18] M. A. Fusella, S. Yang, K. Abbasi, H. H. Choi, Z. Yao, V. Podzorov, A. Avishai, B. P. Rand, Chem. Mater. 2017, 29, 6666.
[19] M. A. Fusella, F. Schreiber, K. Abbasi, J. J. Kim, A. L. Briseno, B. P. Rand, Nano Lett. 2017, 17, 3040.
[20] S. Liu, H. Wu, Z. Xiaotao, W. Hu, Front. Phys. 2021, 16, 13304.
[21] T. Matsukawa, M. Yoshimura, K. Sasai, M. Uchiyama, M. Yamagishi, Y. Tominari, Y. Takahashi, J. Takeya, Y. Kitaoka, Y. Mori, T. Sasaki, J. Cryst. Growth 2010, 312, 310.
[22] P. Irkhin, A. Ryasnyanskiy, M. Koehler, I. Biaggio, Phys Rev B Condens Matter Mater Phys 2012, 86, 085143.
[23] L. Ma, K. Zhang, C. Kloc, H. Sun, M. E. Michel-Beyerle, G. G. Gurzadyan, Phys. Chem. Chem. Phys. 2012, 14, 8307.
[24] H. Kageyama, H. Ohishi, M. Tanaka, Y. Ohmori, Y. Shirota, Appl. Phys. Lett. 2009, 94, 063304.
[25] H. Yang, F. Gajdos, J. Blumberger, J. Phys. Chem. C 2017, 121, 7689.
[26] C. D. Dimitrakopoulos, A. R. Brown, A. Pomp, J. Appl. Phys. 1996, 80, 2501.
[27] C. D. Dimitrakopoulos, P. R. L. Malenfant, Adv. Mater. 2002, 14, 99.
[28] W. C. Germs, K. Guo, R. A. J. Janssen, M. Kemerink, Phys. Rev. Lett. 2012, 109, 016601.
[29] H. Bässler, Phys. Status Solidi 1993, 175, 15.
[30] V. Arkhipov, E. Emelianova, G. Adriaenssens, Phys. Rev. B 2001, 64, 125125.
[31] R. Schmechel, Phys Rev B Condens Matter Mater Phys 2002, 66, 235206.
[32] D. A. Da Silva Filho, E. G. Kim, J. L. Brédas, Adv. Mater. 2005, 17, 1072.
[33] Z. Q. Li, V. Podzorov, N. Sai, M. C. Martin, M. E. Gershenson, M. Di Ventra, D. N. Basov, Phys. Rev. Lett. 2007, 99, 016403.
[34] J. Y. W. Seto, J. Appl. Phys. 1975, 46, 5247.
[35] K. Okuyama, Thin Solid Films 1976, 33, 165.
[36] P. G. Le Comber, W. E. Spear, Phys. Rev. Lett. 1970, 25, 509.
[37] G. D. Cody, T. Tiedje, B. Abeles, B. Brooks, Y. Goldstein, Phys. Rev. Lett. 1981, 47, 1480.
[38] C. H. Qiu, C. Hoggatt, W. Melton, M. W. Leksono, J. I. Pankove, Appl. Phys. Lett. 1995, 2712, 2712.
[39] T. Tiedje, B. Abeles, J. M. Cebulka, Solid State Commun. 1983, 47, 493.
[40] G. Moddel, D. A. Anderson, W. Paul, Phys. Rev. B 1980, 22, 1918.
[41] M. Vaněček, J. Kočka, J. Stuchlík, A. Tříska, Solid State Commun. 1981, 39, 1199.
[42] H. Najafov, B. Lee, Q. Zhou, L. C. Feldman, V. Podzorov, Nat. Mater. 2010, 9, 938.
[43] N. Vagenas, V. Podzorov, P. Kounavis, Phys. Rev. Mater. 2021, 5, 063801.
[44] P. Irkhin, H. Najafov, V. Podzorov, Sci. Rep. 2015, 5, 15323.
[45] W. Y. So, D. V. Lang, V. Y. Butko, X. Chi, J. C. Lashley, A. P. Ramirez, J. Appl. Phys. 2008, 104, 054512.

[46] X. Ren, M. J. Bruzek, D. A. Hanifi, A. Schulzetenberg, Y. Wu, C. H. Kim, Z. Zhang, J. E. Johns, A. Salleo, S. Fratini, A. Troisi, C. J. Douglas, C. D. Frisbie, *Adv. Electron. Mater.* **2017**, *3*, 1700018.

[47] A. Salleo, T. W. Chen, A. R. Völkel, Y. Wu, P. Liu, B. S. Ong, R. A. Street, *Phys Rev B Condens Matter Mater Phys* **2004**, *70*, 115311.

[48] A. L. Foggiatto, Y. Takeichi, K. Ono, H. Suga, Y. Takahashi, M. A. Fusella, J. T. Dull, B. P. Rand, K. Kutsukake, T. Sakurai, *Org. Electron.* **2019**, *74*, 315.

[49] O. Gunawan, Y. Virgus, K. F. Tai, *Appl. Phys. Lett.* **2015**, *106*, 062407.

[50] O. Gunawan, M. Pereira, *Rotating magnetic field Hall measurement system. US Patent 9* **2017**, *772*, 385.

[51] J. Takeya, M. Yamagishi, Y. Tominari, R. Hirahara, Y. Nakazawa, T. Nishikawa, T. Kawase, T. Shimoda, S. Ogawa, *Appl. Phys. Lett.* **2007**, *90*, 102120.

[52] O. Gunawan, S. R. Pae, D. M. Bishop, Y. Virgus, J. H. Noh, N. J. Jeon, Y. S. Lee, X. Shao, T. Todorov, D. B. Mitzi, B. Shin, *Nature* **2019**, *575*, 151.

[53] V. Bruevich, H. H. Choi, V. Podzorov, *Adv. Funct. Mater.* **2021**, *31*, 2006178.

[54] S. Z. Bisri, T. Takenobu, T. Takahashi, Y. Iwasa, *Appl. Phys. Lett.* **2010**, *96*, 183304.

[55] H. M. Lee, H. Moon, H. S. Kim, Y. N. Kim, S. M. Choi, S. Yoo, S. O. Cho, *Org. Electron.* **2011**, *12*, 1446.

[56] S.-J. Wang, M. Sawatzki, H. Kleemann, I. Lashkov, D. Wolf, A. Lubk, F. Talnack, S. Mannsfeld, Y. Krupskaya, B. Büchner, K. Leo, *Mater Today Phys* **2021**, *17*, 100352.

[57] H. H. Choi, A. F. Paterson, M. A. Fusella, J. Panidi, O. Solomeshch, N. Tessler, M. Heeney, K. Cho, T. D. Anthopoulos, B. P. Rand, V. Podzorov, *Adv. Funct. Mater.* **2019**, *30*, 1903617.

[58] H. T. Yi, Y. N. Gartstein, V. Podzorov, *Sci. Rep.* **2016**, *6*, 23650.

[59] L. Friedman, *Philos. Mag. B Phys. Condens. Matter; Stat. Mech. Electron. Opt. Magn. Prop.* **1978**, *38*, 467.

[60] J. F. Chang, T. Sakanoue, Y. Olivier, T. Uemura, M. B. Dufourg-Madec, S. G. Yeates, J. Cornil, J. Takeya, A. Troisi, H. Sirringhaus, *Phys. Rev. Lett.* **2011**, *107*, 066601.

[61] H. Tamura, M. Tsukada, H. Ishii, N. Kobayashi, K. Hirose, *Phys Rev B Condens Matter Mater Phys* **2013**, *87*, 2.

[62] Y. Chen, H. T. Yi, V. Podzorov, *Phys. Rev. Appl.* **2016**, *5*, 034008.

[63] S. P. Senanayak, A. Z. Ashar, C. Kanimozhi, S. Patil, K. S. Narayan, *Phys Rev B Condens Matter Mater Phys* **2015**, *91*, 115302.

[64] P. G. Le Comber, D. I. Jones, W. E. Spear, *Philos. Mag.* **1977**, *35*, 1173.

[65] J. Kakalios, *J Non Cryst Solids* **1989**, *114*, 372.

[66] S. Wang, M. Ha, M. Manno, C. D. Frisbie, C. Leighton, *Nat. Commun.* **2012**, *3*, 1210.

[67] V. Rani, P. Kumar, A. Sharma, S. Yadav, B. Singh, N. Ray, S. Ghosh, *Sci. Rep.* **2019**, *9*, 20193.

[68] M. Ito, Y. Yamashita, T. Mori, K. Ariga, J. Takeya, S. Watanabe, *App. Phys. Lett.* **2021**, *119*, 013302.

[69] M. Gobbi, E. Orgiu, *J. Mater. Chem. C* **2017**, *5*, 5572.

[70] W. Wagemans, B. Koopmans, *Phys. Status Solidi Basic Res.* **2011**, *248*, 1029.

[71] K. M. Alam, S. C. Bodepudi, R. Starko-Bowes, S. Pramanik, *Appl. Phys. Lett.* **2012**, *101*, 192403.

[72] P. A. Bobbert, T. D. Nguyen, F. W. A. Van Oost, B. Koopmans, M. Wohlgenannt, *Phys. Rev. Lett.* **2007**, *99*, 216801.

[73] B. Movaghar, L. Schweitzer, *J. Phys. C: Solid State Phys.* **1978**, *11*, 125.

[74] I. I. Fishchuk, A. K. Kadashchuk, J. Genoe, V. N. Poroshin, H. Bässler, *Mol. Cryst. Liq. Cryst.* **2011**, *535*, 1.

[75] S. Seo, B. N. Park, P. G. Evans, *Appl. Phys. Lett.* **2006**, *88*, 232114.

[76] B. Park, I. In, P. Gopalan, P. G. Evans, S. King, P. F. Lyman, *Appl. Phys. Lett.* **2008**, *92*, 90.

[77] C. Liu, K. Huang, W. T. Park, M. Li, T. Yang, X. Liu, L. Liang, T. Minari, Y. Y. Noh, *Mater. Horiz.* **2017**, *4*, 608.

[78] Y. Hu, L. Jiang, Q. Chen, J. Guo, Z. Chen, *J. Phys. Chem. Lett.* **2018**, *9*, 2869.

[79] S. Fratini, D. Mayou, S. Ciuchi, *Adv. Funct. Mater.* **2016**, *26*, 2292.

[80] A. Troisi, G. Orlandi, *Phys. Rev. Lett.* **2006**, *96*, 086601.

[81] D. Balzer, T. J. A. M. Smolders, D. Blyth, S. N. Hood, I. Kassal, *Chem. Sci.* **2021**, *12*, 2276.

[82] J. E. Anthony, *Chem. Rev.* **2006**, *106*, 5028.

[83] L. Luo, G. Liu, L. Huang, X. Cao, M. Liu, H. Fu, J. Yao, *Appl. Phys. Lett.* **2009**, *95*, 2007.

[84] R. Noriega, J. Rivnay, K. Vandewal, F. P. V. Koch, N. Stingelin, P. Smith, M. F. Toney, A. Salleo, *Nat. Mater.* **2013**, *12*, 1038.

[85] O. G. Ziogos, S. Giannini, M. Ellis, J. Blumberger, *J. Mater. Chem. C* **2020**, *8*, 1054.

[86] L. Zhang, A. Fonari, Y. Liu, A. M. Hoyt, H. Lee, D. Granger, S. Parkin, T. P. Russell, J. E. Anthony, J. Bredas, V. Coropceanu, *J Am Chem Soc* **2014**, *136*, 9248.

[87] K. J. Thorley, M. Benford, Y. Song, S. R. Parkin, C. Risko, J. E. Anthony, *Mater. Adv.* **2021**, *2*, 5415.

[88] J. E. Anthony, J. S. Brooks, D. L. Eaton, S. R. Parkin, *J. Am. Chem. Soc.* **2001**, *123*, 9482.

[89] S. Thomas, H. Li, R. R. Dasari, A. M. Evans, I. Castano, T. G. Allen, O. G. Reid, G. Rumbles, W. R. Dichtel, N. C. Gianneschi, S. R. Marder, V. Coropceanu, J. L. Brédas, *Mater. Horiz.* **2019**, *6*, 1868.

[90] S. Fu, E. Jin, H. Hanayama, W. Zheng, H. Zhang, L. Di Virgilio, M. A. Addicoat, M. Mezger, A. Narita, M. Bonn, K. Müllen, H. I. Wang, *J. Am. Chem. Soc.* **2022**, *144*, 7489.

[91] R. Liu, K. T. Tan, Y. Gong, Y. Chen, Z. Li, S. Xie, T. He, Z. Lu, H. Yang, D. Jiang, *Chem. Soc. Rev.* **2021**, *50*, 120.

[92] S. Wang, M. Sawatzki, G. Darbandy, F. Talnack, J. Vahland, M. Malfois, A. Kloes, S. Mannsfeld, H. Kleemann, K. Leo, *Nature* **2022**, *606*, 700.

[93] J. Euvrard, B. P. Rand, *Nature* **2022**, *606*, 661.

[94] M. T. Sajjad, A. Ruseckas, I. D. W. Samuel, *Matter* **2020**, *3*, 341.